Computation of Transfer Maps from Surface Data with Applications to Wigglers

Using Elliptical Cylinders

Chad Mitchell and Alex Dragt
University of Maryland

March 2006 Version

Abstract

Simulations indicate that the dynamic aperture of proposed ILC Damping Rings is dictated primarily by the nonlinear properties of their wiggler transfer maps. Wiggler transfer maps in turn depend sensitively on fringe-field and high-multipole effects. Therefore it is important to have detailed magnetic field data including knowledge of high spatial derivatives. This talk describes how such information can be extracted reliably from 3-dimensional field data on a grid as provided, for example, by various 3-dimensional field codes available from Vector Fields. The key ingredient is the use of surface data and the smoothing property of the inverse Laplacian operator.

Objective

- To obtain an accurate representation of the wiggler field that is analytic and satisfies Maxwell equations exactly. We want a vector potential that is analytic and $\nabla \times \nabla \times \boldsymbol{A} = 0$.

- Use B-V data to find an accurate series representation of interior vector potential through order N in (x,y) deviation from design orbit.

$$A_x(x,y,z) = \sum_{l=1}^{L} a_l^x(z) P_l(x,y)$$

L=27 for N=6

- Use a Hamiltonian expressed as a series of homogeneous polynomials

$$K = -\sqrt{\frac{(p_t + q\phi)^2}{c^2} - (\vec{p}_\perp - q\vec{A}_\perp)^2} - qA_z = \sum_{s=1}^{S} h_s(z) K_s(x, p_x y, p_y, \tau, p_\tau)$$

S=923 for N=6

- We compute the design orbit and the transfer map about the design orbit to some order. We obtain a factorized symplectic map for single-particle orbits through the wiggler:

$$M = R_2 e^{:f_3:} e^{:f_4:} e^{:f_5:} e^{:f_6:} \ldots$$

Fitting Wiggler Data

- Data on regular Cartesian grid

4.8cm in x, dx=0.4cm

2.6cm in y, dy=0.2cm

480cm in z, dz=0.2cm

- Field components Bx, By, Bz in one quadrant given to a precision of 0.05G.

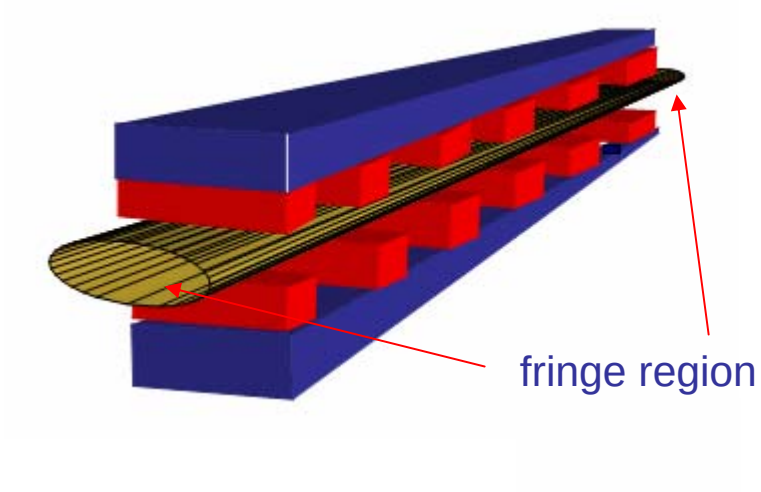

- Place an imaginary elliptic cylinder between pole faces, extending beyond the ends of the magnet far enough that the field at the ends is effectively zero.

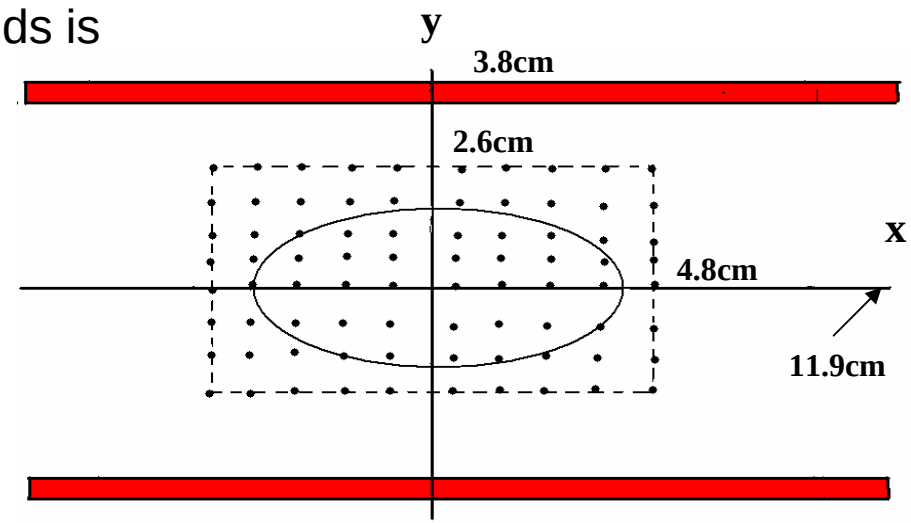

- Fit data onto elliptic cylindrical surface using bicubic interpolation to obtain the normal component on the surface.

- Compute the interior vector potential and all its desired derivatives from surface data.

Elliptic Coordinates

Defined by relations:

$$x = f \cosh u \cos v$$
$$y = f \sinh u \sin v$$

where f=a (distance from origin to focus).

Letting z=x+iy, w=u+iv we have

$$z = \Im(w) = f \cosh w$$

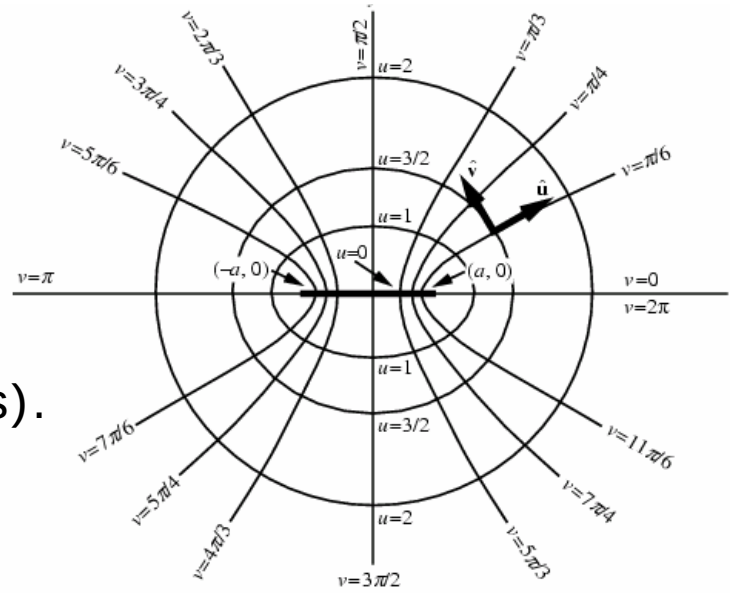

Jacobian:

$$J(u,v) = \left|\Im'(z)\right| = \left|f \sinh z\right| = f(\sinh^2 u + \sin^2 v)$$

Laplacian:

$$\nabla^2 = \frac{1}{J(u,v)}\left(\frac{\partial^2}{\partial u^2} + \frac{\partial}{\partial v^2}\right) + \frac{\partial^2}{\partial z^2}$$

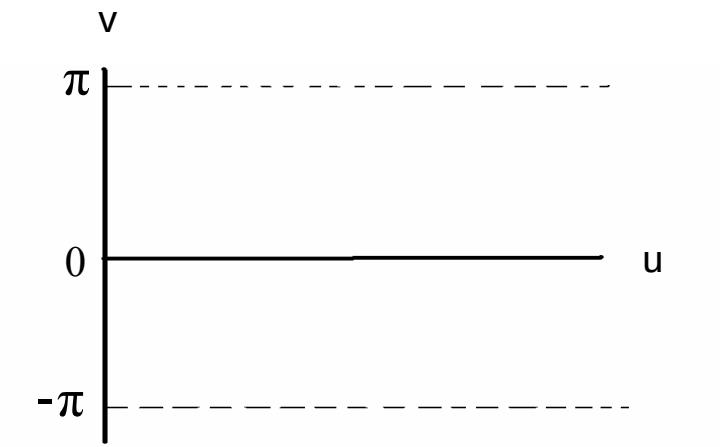

- Fitting done in a source-free region, so we can use a scalar potential satisfying $(\nabla_\perp^2 - k^2)\tilde{\psi}(u,v,k) = 0$ where

$$\psi(x,y,z) = \int_{-\infty}^{\infty} dk e^{ikz} \tilde{\psi}(x,y,k)$$

- Search for product solutions in elliptic coordinates $\tilde{\psi} \propto U(u)V(v)$

- Then we find that V and U satisfy the Mathieu Equations

$$\frac{d^2V}{dv^2} + [\lambda - 2q\cos(2v)]V = 0$$

$$\frac{d^2U}{du^2} - [\lambda - 2q\cosh(2u)]U = 0,$$

with $q = -\frac{k^2 f^2}{4}.$

- Periodicity in v forces $\lambda(q)$ to have certain characteristic values $\lambda = a_m(q)$ and $\lambda = b_m(q)$.

The solutions for V are

Mathieu functions

$ce_m(v,q)$ ⟵ even in v

$se_m(v,q)$ ⟵ odd in v

where $q = -\dfrac{k^2 f^2}{4}$

The associated solutions for U are

Modified Mathieu functions

$$Ce_m(u,q) = ce_m(iu,q),$$
$$Se_m(u,q) = -ise_m(iu,q).$$

For $\widetilde{\Psi}(x,y,k)$ we make the Ansatz

$$\widetilde{\psi}(x,y,k) = \sum_{n=0}^{\infty}\left[\left(\frac{F_n(k)}{Se_n'(u_b,k)}\right)Se_n(u,k)se_n(v,k) + \left(\frac{G_n(k)}{Ce_n'(u_b,k)}\right)Ce_n(u,k)ce_n(v,k)\right].$$

Boundary-Value Solution

- Normal component of field on bounding surface defines a Neumann problem with interior field determined by angular Mathieu expansion on the boundary:

$$B_u(v,k) = \partial_u \tilde{\psi} = \sum_{n=0}^{\infty} F_n(k) se_n(v,k) + G_n(k) ce_n(v,k)$$

- Angular Mathieu coefficients $F_n(k), G_n(k)$ on boundary are integrated against a kernel that falls off rapidly with large k, minimizing the contribution of high-frequency noise.

- On-axis gradients are found that specify the field and its derivatives.

- Power series representation in (x,y)

$$A_{\begin{Bmatrix} x \\ y \end{Bmatrix}} = \sum_{m=1}^{\infty}\sum_{l=0}^{\infty} \frac{(-1)^l (m-1)!}{2^{2l}\, l!(l+m)!} \begin{Bmatrix} x \\ y \end{Bmatrix} (x^2+y^2)^l \left[\mathrm{Re}(x+iy)^m C_{m,s}^{[2l+1]}(z) - \mathrm{Im}(x+iy)^m C_{m,c}^{[2l+1]}(z) \right]$$

$$A_z = \sum_{m=1}^{\infty}\sum_{l=0}^{\infty} \frac{(-1)^l (2l+m)(m-1)!}{2^{2l}\, l!(l+m)!} (x^2+y^2)^l \left[-\mathrm{Re}(x+iy)^m C_{m,s}^{[2l]}(z) + \mathrm{Im}(x+iy)^m C_{m,c}^{[2l]}(z) \right]$$

- The vertical field then takes the form:

$$B_y = C_1(z) + 3C_3(z)(x^2 - y^2) - \frac{1}{8}C_1^{[2]}(z)(x^2 + 3y^2)$$
$$+ \frac{1}{192}C_1^{[4]}(z)(x^4 + 6x^2y^2 + 5y^4) - \frac{1}{16}C_3^{[2]}(z)(3x^4 + 6x^2y^2 - 5y^4)$$
$$+ C_5(z)(5x^4 - 30x^2y^2 + 5y^4) + O(x, y)^5$$

- With similar expressions for the other components of $\mathbf{B}$ and the components of $\mathbf{A}$.

Dipole Field Test

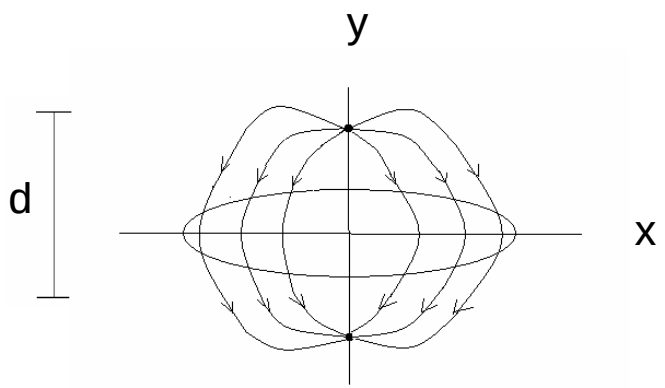

- Simple field configuration in which scalar potential, field, elliptical moments, and on-axis gradients can be determined analytically.
- Tested for two different aspect ratios: 4:3 and 5:1.

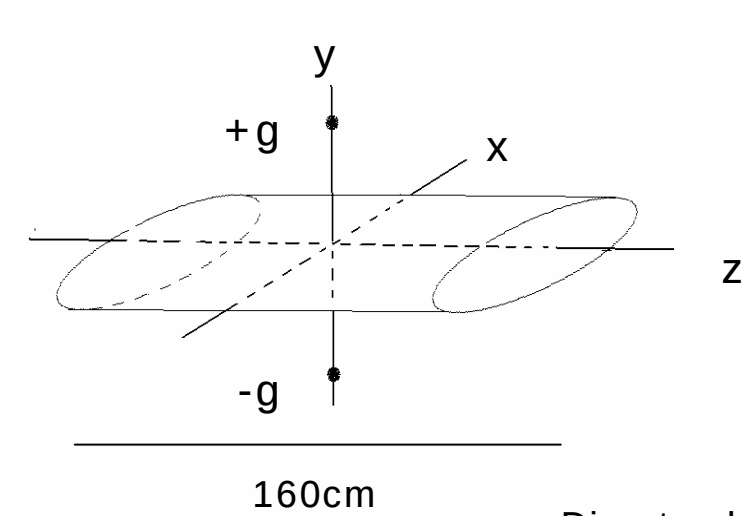

Pole location: d=4.7008cm

Pole strength: g=0.3Tcm^2

Semimajor axis: 1.543cm/4.0cm

Semiminor axis: 1.175cm/0.8cm

Boundary to pole: 3.526cm/3.9cm

Focal length: f=1.0cm/3.919cm

Bounding ellipse: u=1.0/0.2027

Direct solution for interior scalar potential
accurate to 3*10-10: set by convergence/roundoff
Computation of on-axis gradients C1, C3, C5
accurate to 2*10-10 before final Fourier transform
accurate to 2.6*10-9 after final Fourier transform

Fit to the Proposed ILC Wiggler Field Using Elliptical Cylinder

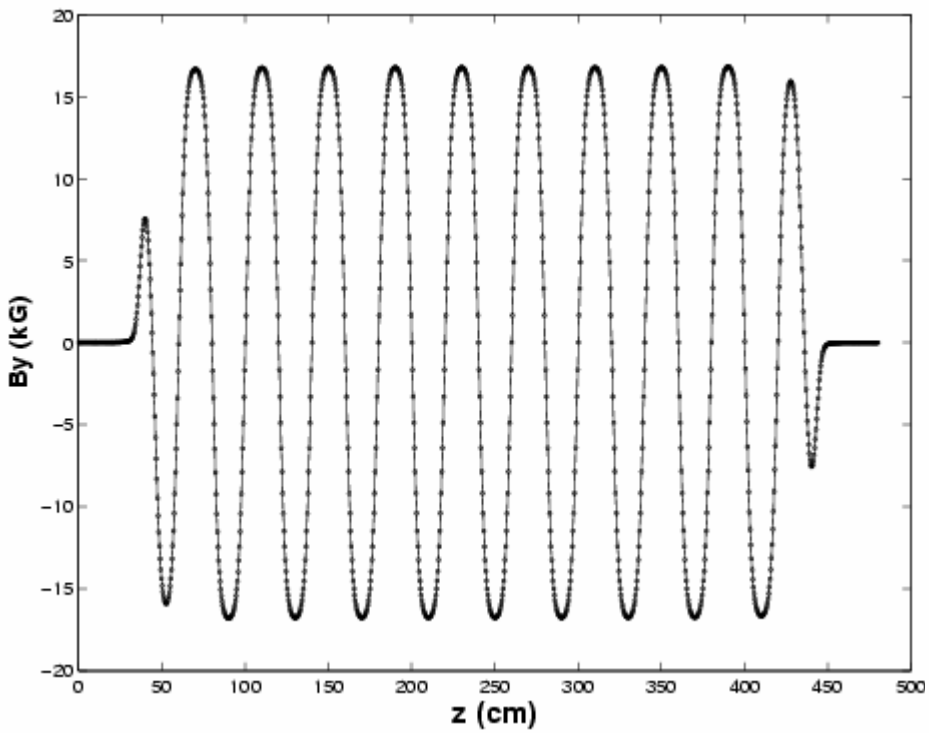

Fit to vertical field By
at x=0.4cm, y=0.2cm.

Note precision of data.

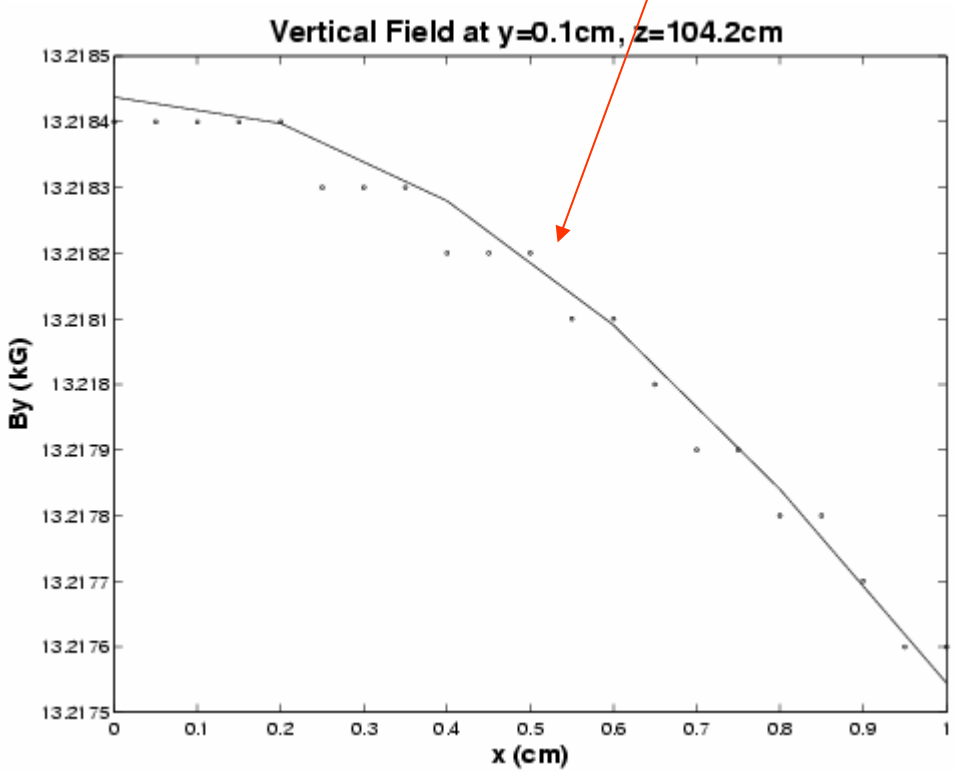

Fit to the Proposed ILC Wiggler Field Using Elliptical Cylinder

No information about Bz was used to create this plot.

Fit to longitudinal field Bz at x=0.4cm, y=0.2cm.

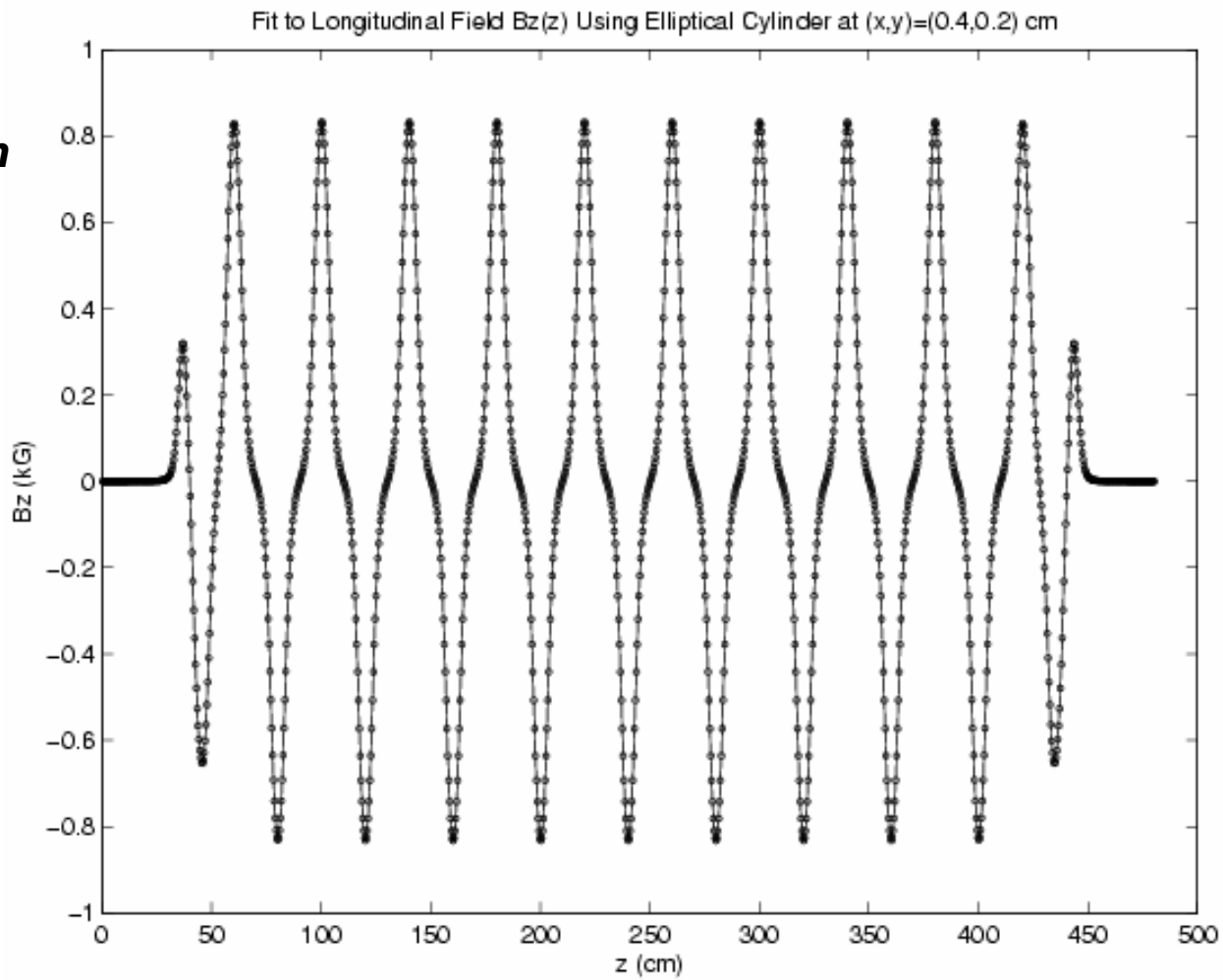

Residuals of fit to Cornell field data: field peaks near 17kG

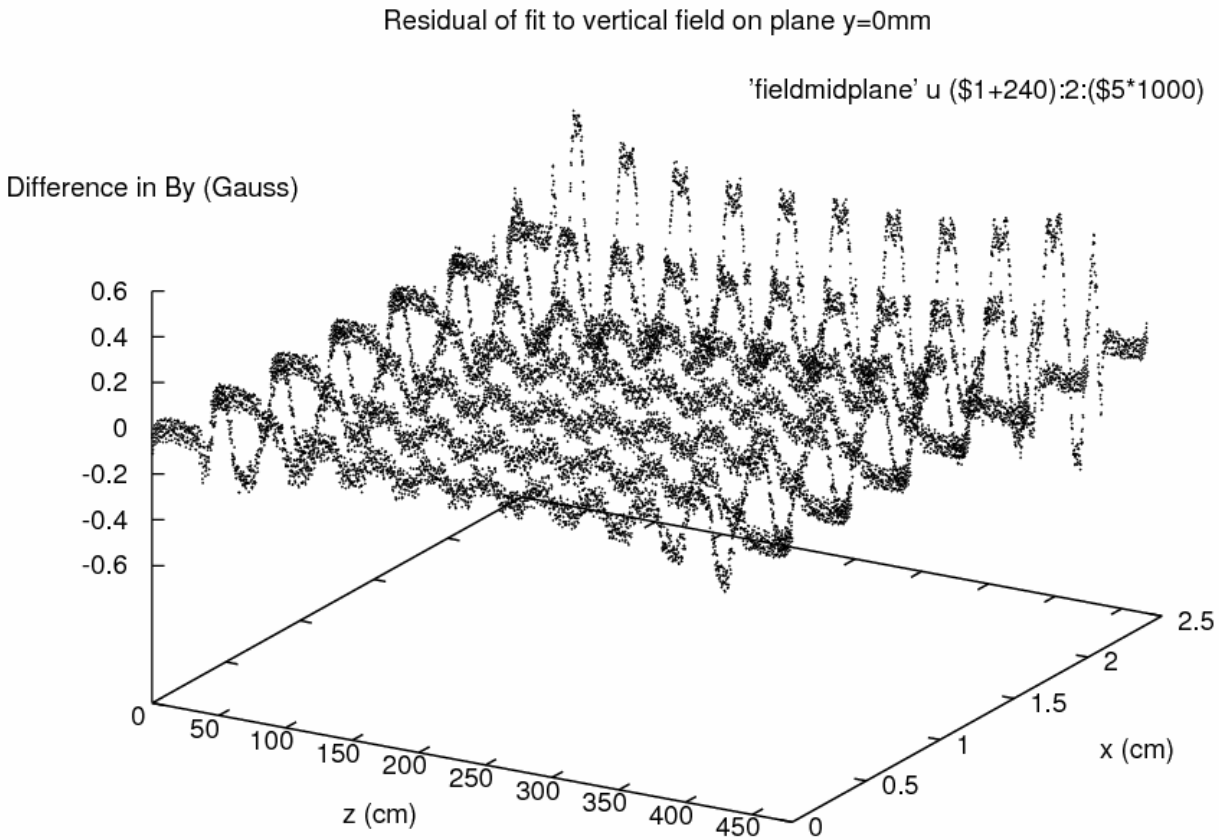

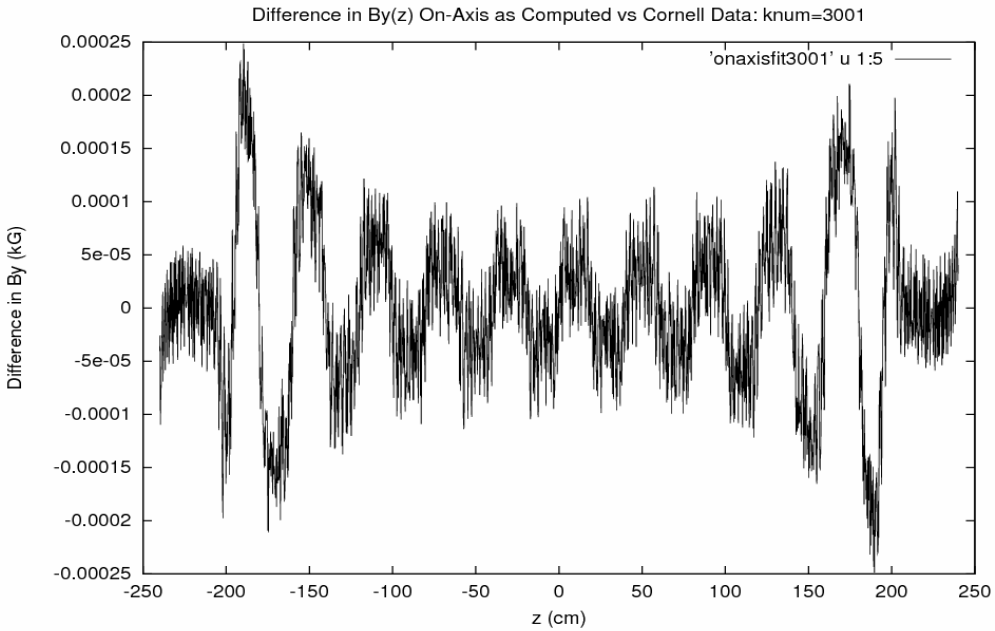
Difference in By(z) On-Axis as Computed vs Cornell Data: knum=3001
'onaxisfit3001' u 1:5
Difference in By (kG)
z (cm)
0.00025
0.0002
0.00015
0.0001
5e-05
0
-5e-05
-0.0001
-0.00015
-0.0002
-0.00025
-250
-200
-150
-100
-50
0
50
100
150
200
250

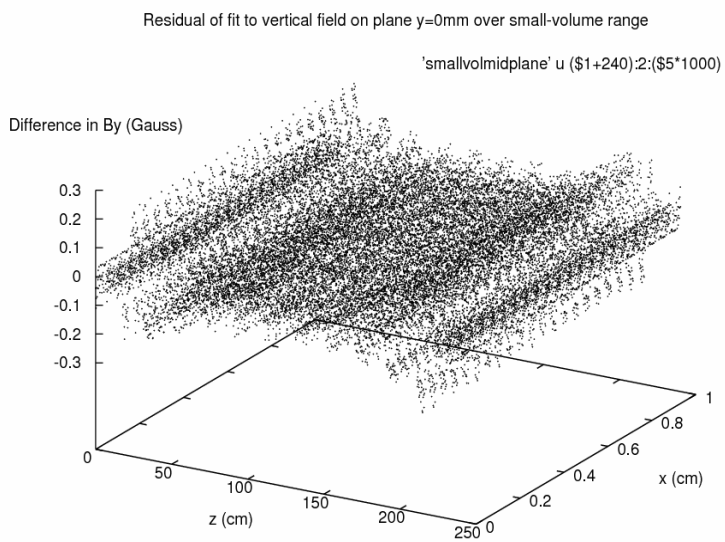
Residual of fit to vertical field on plane y=0mm over small-volume range
'smallvolmidplane' u ($1+240):2:($5*1000)
Difference in By (Gauss)
0.3
0.2
0.1
0
-0.1
-0.2
-0.3
0
50
100
150
200
250
z (cm)
0
0.2
0.4
0.6
0.8
1
x (cm)

Reference orbit through proposed ILC wiggler at 5 GeV

Maximum deviation 0.6 mm

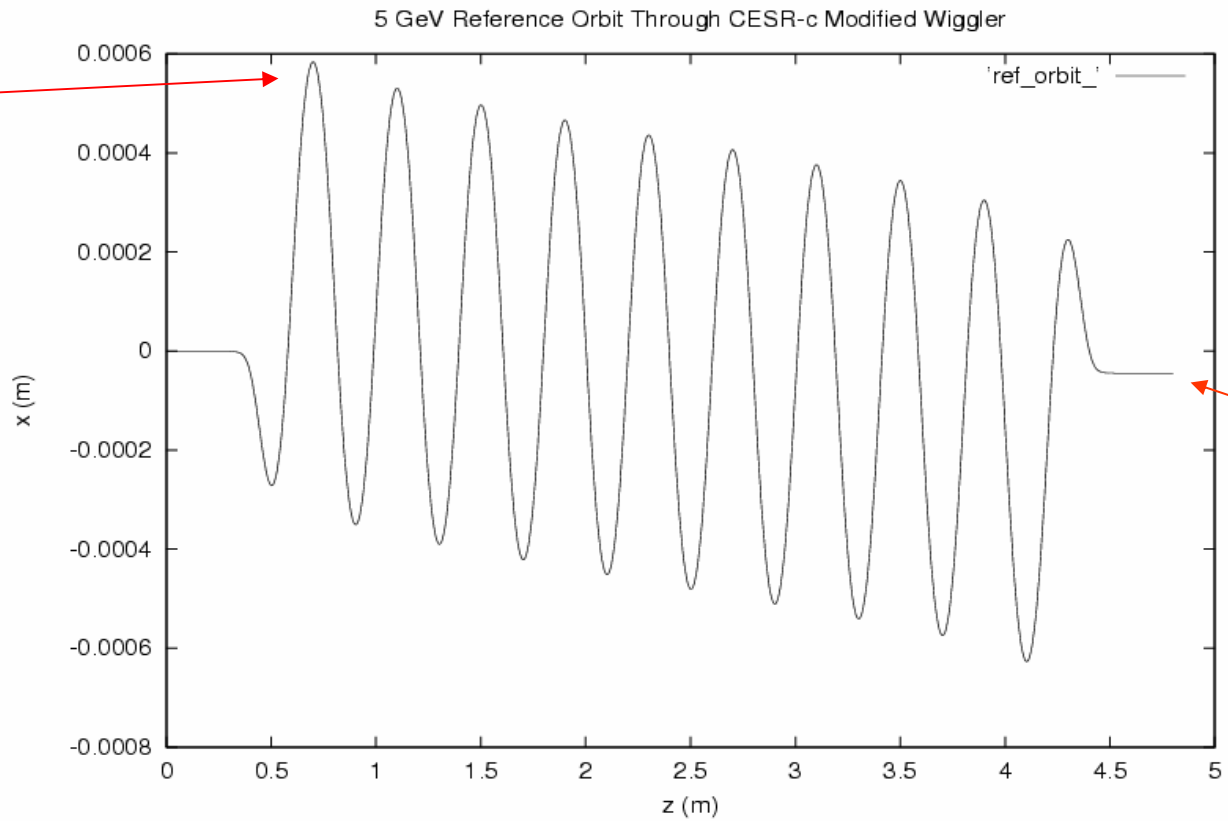

Exit displacement

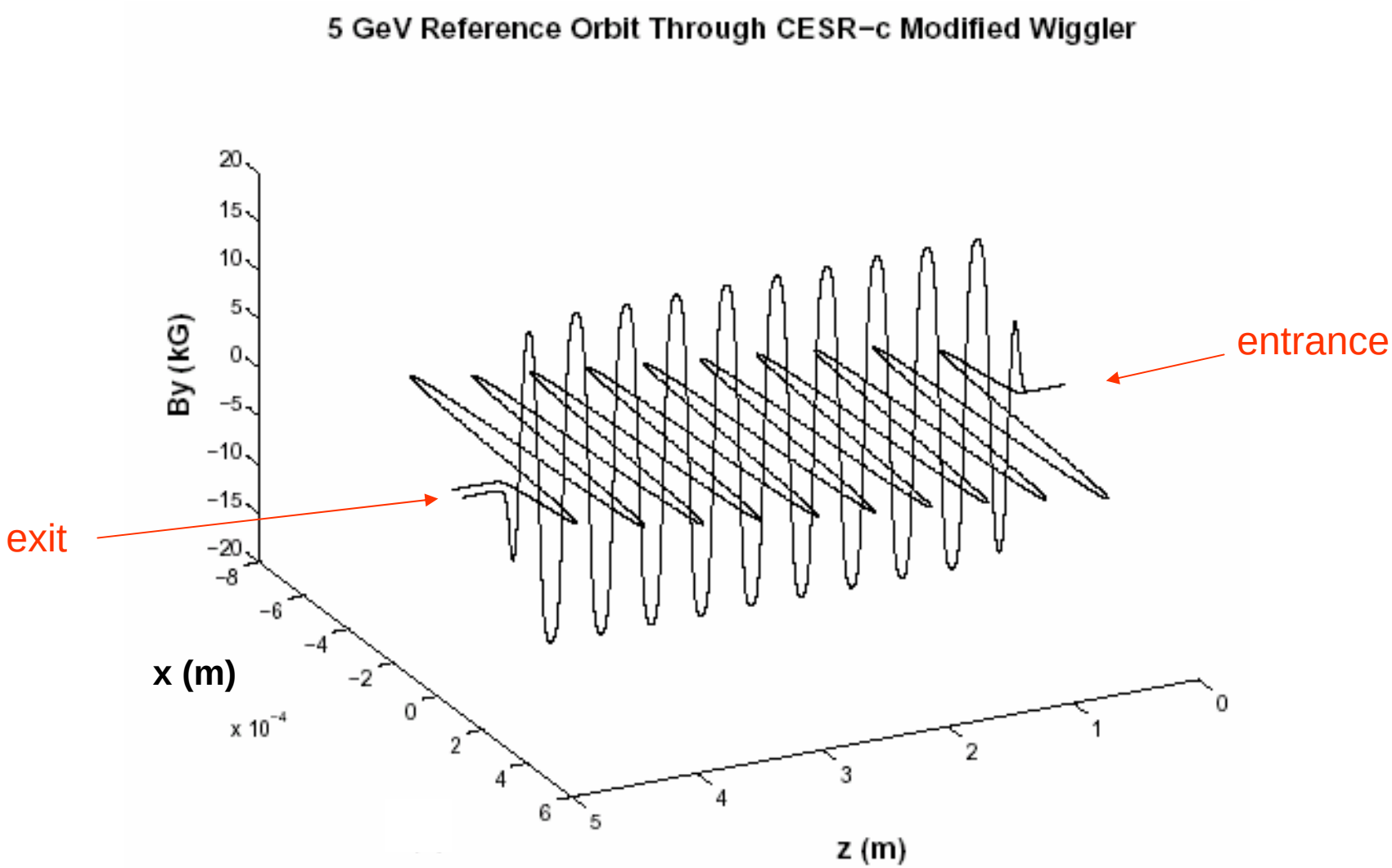
5 GeV Reference Orbit Through CESR−c Modified Wiggler
By (kG)
20
15
10
5
0
−5
−10
−15
−20
−8
−6
−4
−2
0
2
4
6
x (m)
x 10^−4
5
4
3
2
1
0
z (m)
entrance
exit

Phase space trajectory of 5 GeV on-axis reference particle

Mechanical momentum

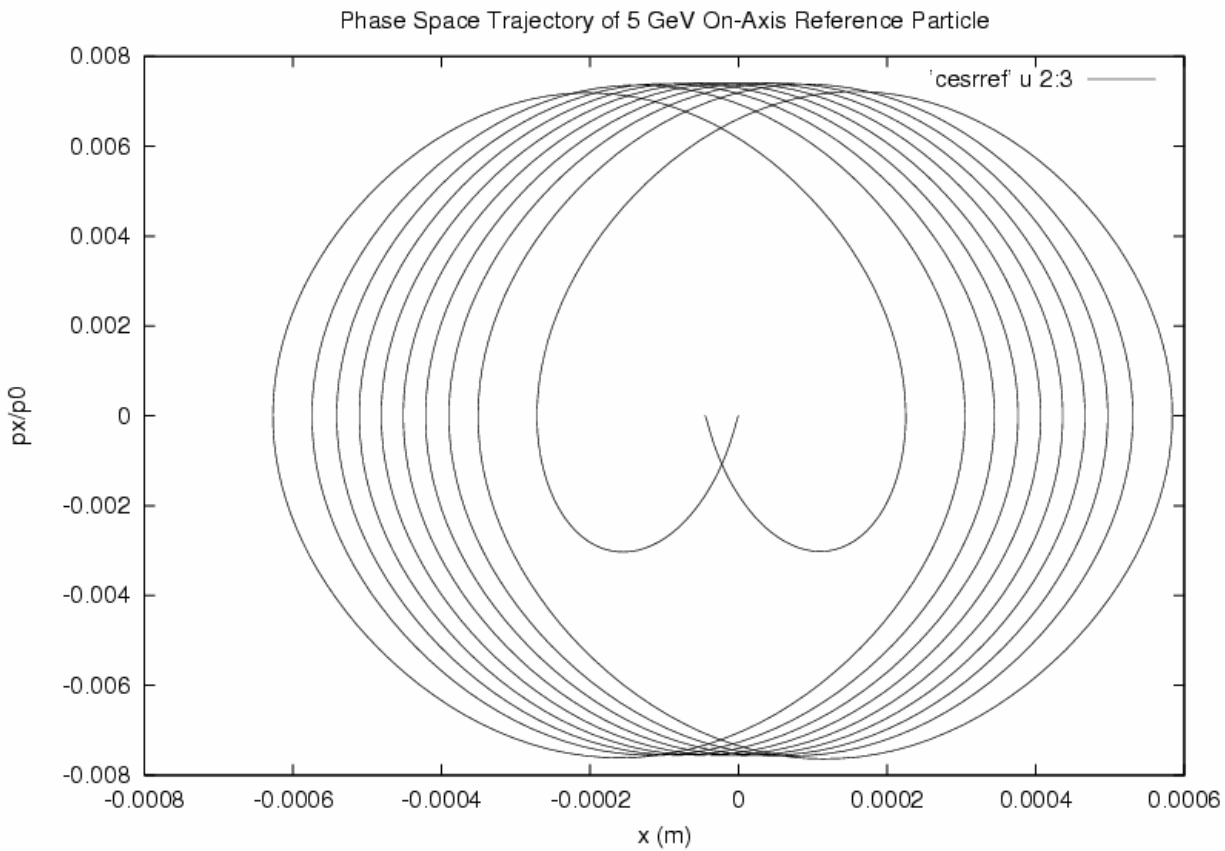

X (m)

Ray trace for proposed ILC wiggler

Result of numerical integration for several 5 GeV rays with normal entry.

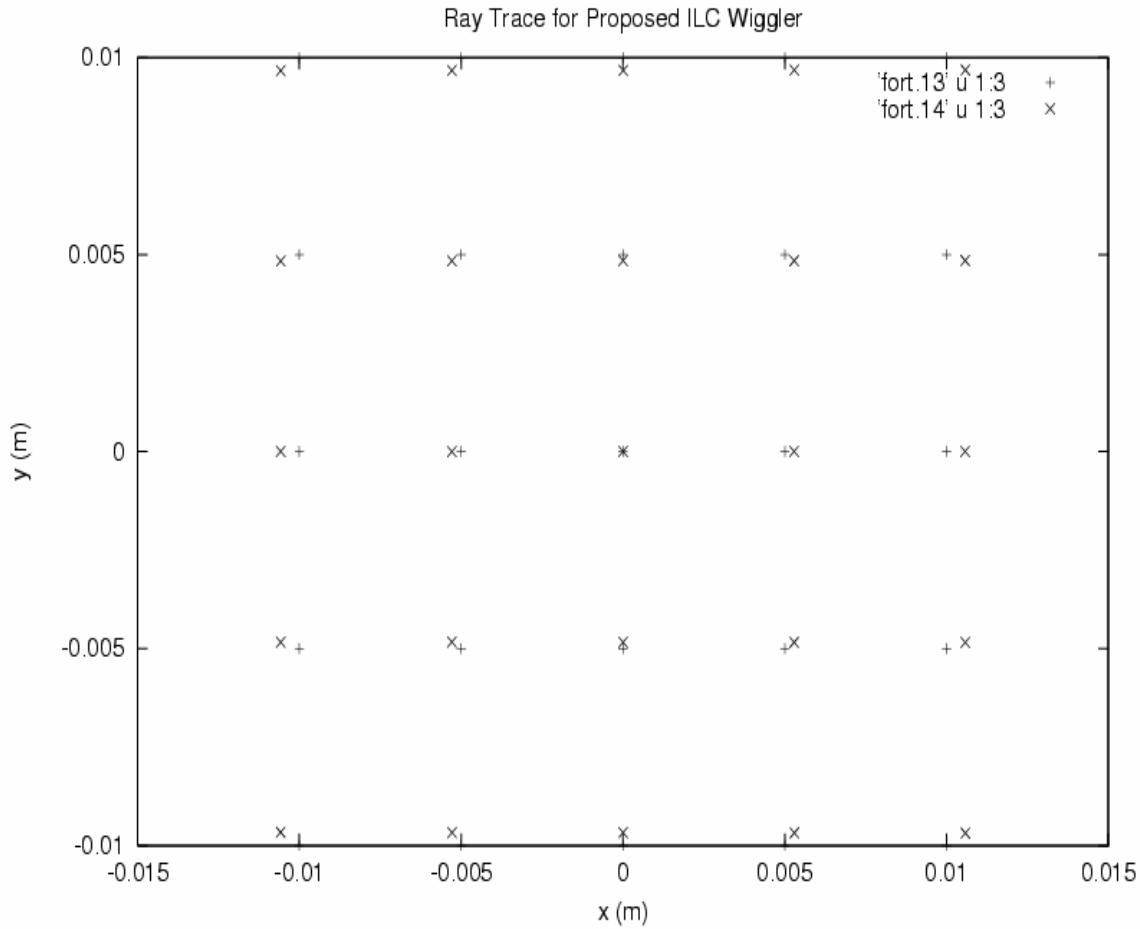

Initial grid of spacing 5mm in the xy plane.

+ initial values, x final values.

Defocusing in x, focusing in y

REFERENCE ORBIT DATA

At entrance:

x (m) = 0.000000000000000E+000
can. momentum p_x = 0.000000000000000E+000
mech. momentum p_x = 0.000000000000000E+000
y (m) = 0.000000000000000E+000
mech. momentum p_y = 0.000000000000000E+000
angle phi_x (rad) = 0.000000000000000E+000
time (s) = 0.000000000000000E+000
p_t/(p0c) = -1.0000000052213336

At exit:

x (m) = -4.534523825505101E-005
can. momentum p_x = 1.245592900543683E-007
mech. momentum p_x = 1.245592900543683E-007
y (m) = 0.000000000000000E+000
mech. momentum p_y = 0.000000000000000E+000
angle phi_x (rad) = 1.245592900543687E-007
time of flight (s) = 1.60112413288E-008
p_t/(p0c) = -1.0000000052213336

Bending angle (rad) = 1.245592900543687E-007

****

matrix for map is :

1.05726E+00	4.92276E+00	0.00000E+00	0.00000E+00	0.00000E+00	-5.43908E-05
2.73599E-02	1.07323E+00	0.00000E+00	0.00000E+00	0.00000E+00	-4.82684E-06
0.00000E+00	0.00000E+00	9.68425E-01	4.74837E+00	0.00000E+00	0.00000E+00
0.00000E+00	0.00000E+00	-1.14609E-02	9.76409E-01	0.00000E+00	0.00000E+00
3.61510E-06	-3.46126E-05	0.00000E+00	0.00000E+00	1.00000E+00	9.87868E-05
0.00000E+00	0.00000E+00	0.00000E+00	0.00000E+00	0.00000E+00	1.00000E+00

nonzero elements in generating polynomial are :

f(28)=f(30 00 00)=-0.86042425633623D-03
f(29)=f(21 00 00)= 0.56419178301165D-01
f(33)=f(20 00 01)=-0.76045220664105D-03
f(34)=f(12 00 00)=-0.25635788141484D+00

. . . . Currently through f(923) – degree 6.

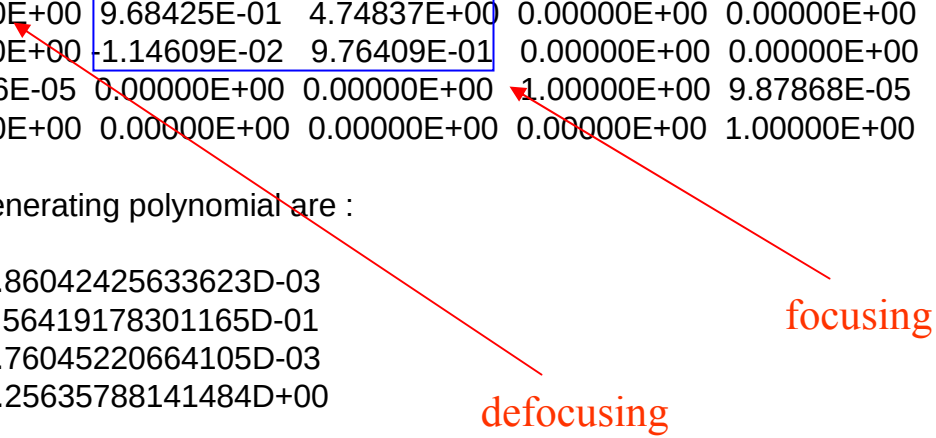

Alternative Wiggler Field Fitting Techniques

- The model form used for the wiggler field fitting by Cornell is written as:

$$\mathbf{B}_{fit} = \sum_{n=1}^{N} \mathbf{B}_n(x, y, s; C_n, k_{xn}, k_{sn}, \phi_{sn}, f_n)$$

where each term is written in one of three forms. For the present wiggler, each term is of the form:

$$B_x = -C\frac{k_x}{k_y}\sin(k_x x)\sinh(k_y y)\cos(k_s z + \phi_s)$$

$$B_y = C\cos(k_x x)\cosh(k_y y)\cos(k_s s + \phi_s) \qquad \text{with} \quad k_y^2 = k_x^2 + k_s^2$$

$$B_z = -C\frac{k_s}{k_y}\cos(k_x x)\sinh(k_y y)\sin(k_s s + \phi_s)$$

- The set of parameters $\{C_n, k_{xn}, k_{sn}, \phi_{sn} : n = 1,..., N\}$ is allowed to vary continuously, in such a way as to minimize the merit function:

$$M = \sum_{data\_pts} \left|\mathbf{B}_{fit} - \mathbf{B}_{data}\right|^2 + w_c \sum_{n=1}^{N} |C_n|$$

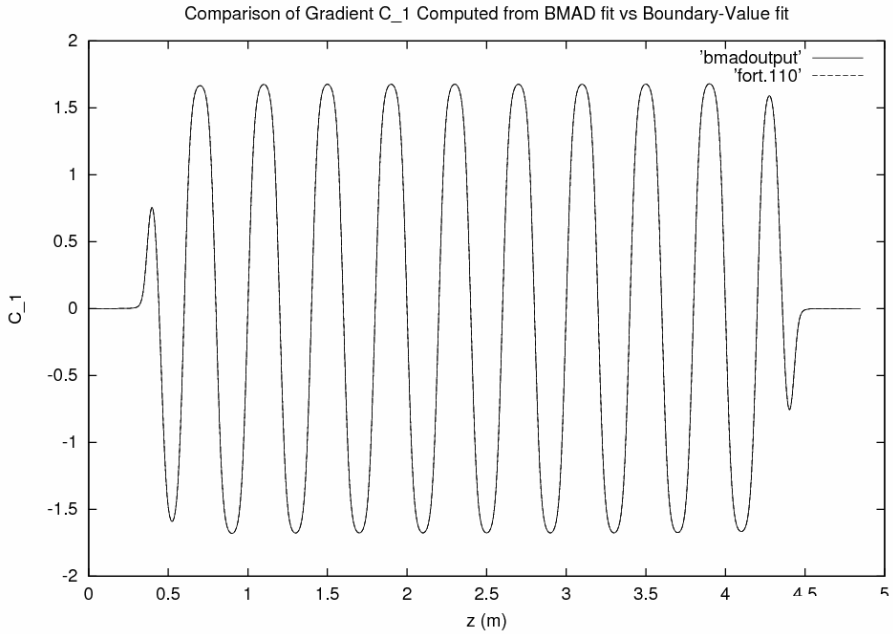

Comparison of on-axis gradient C_1 with the gradient obtained from Cornell's field fit

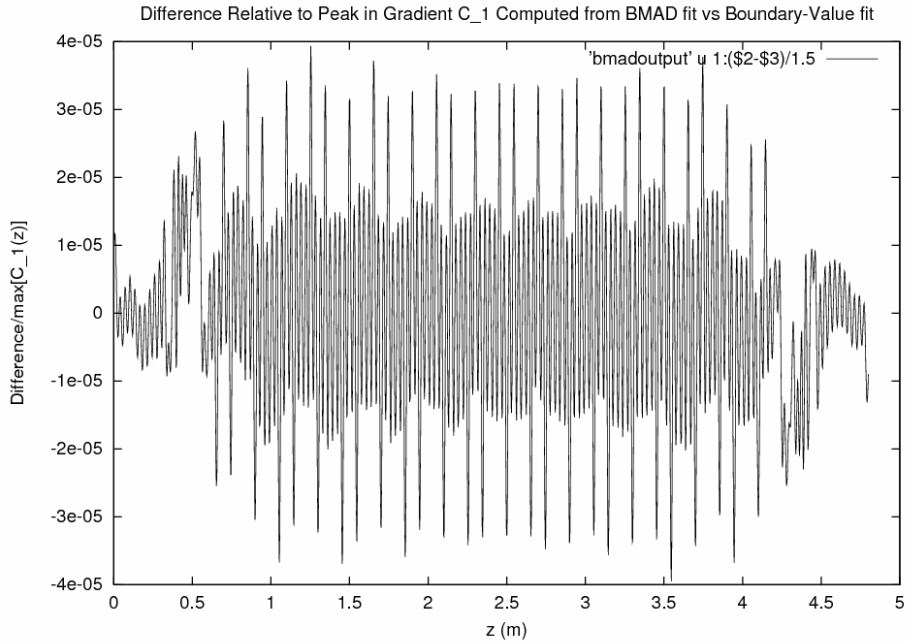

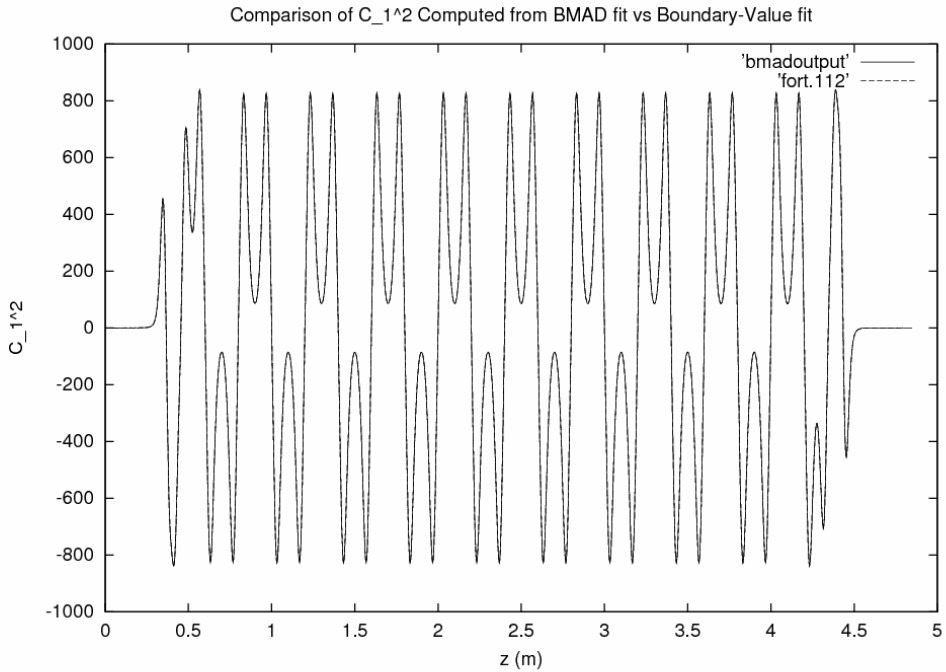

Comparison of on-axis gradient $C_1^{[2]}$ with the gradient obtained from Cornell's field fit

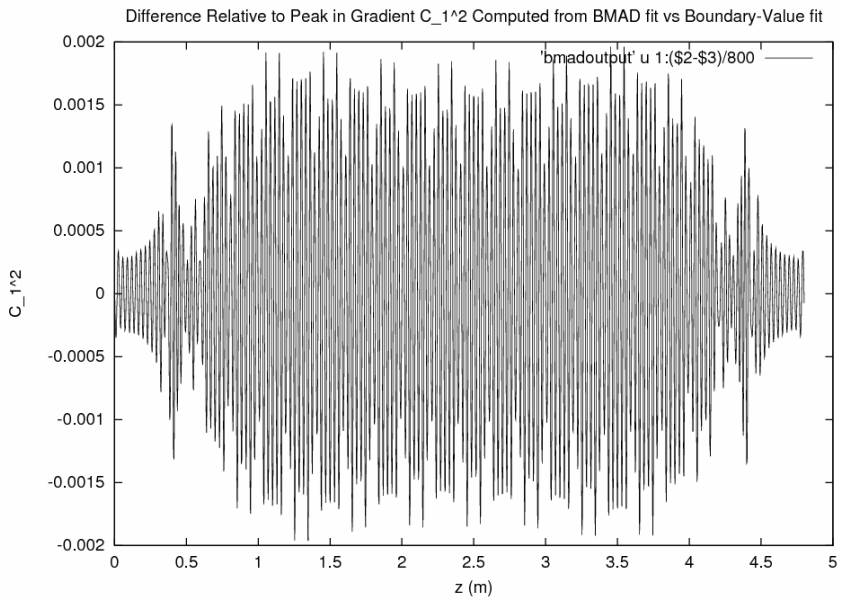

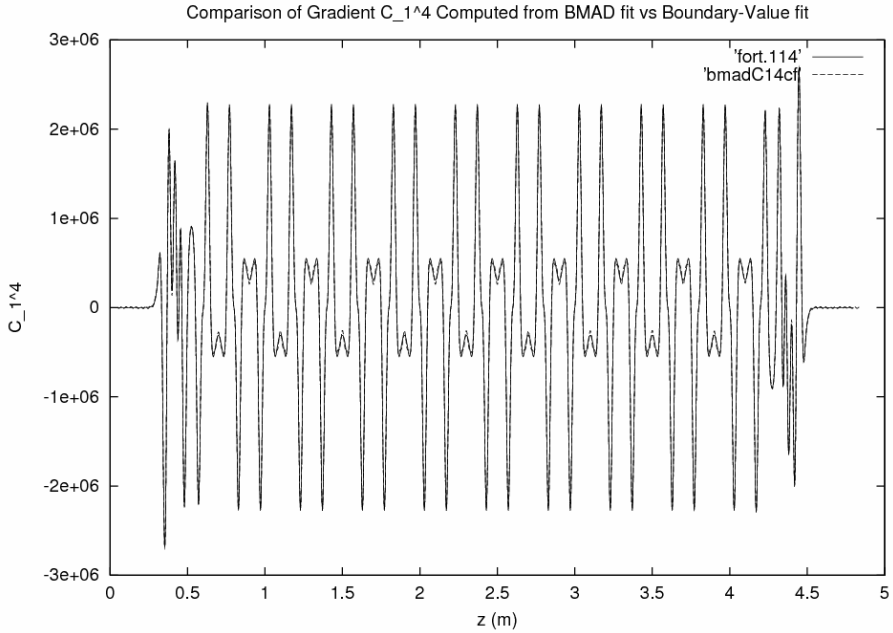
Comparison of Gradient C_1^4 Computed from BMAD fit vs Boundary-Value fit
'fort.114'
'bmadC14cff'
C_1^4
z (m)
3e+06
2e+06
1e+06
0
-1e+06
-2e+06
-3e+06
0
0.5
1
1.5
2
2.5
3
3.5
4
4.5
5

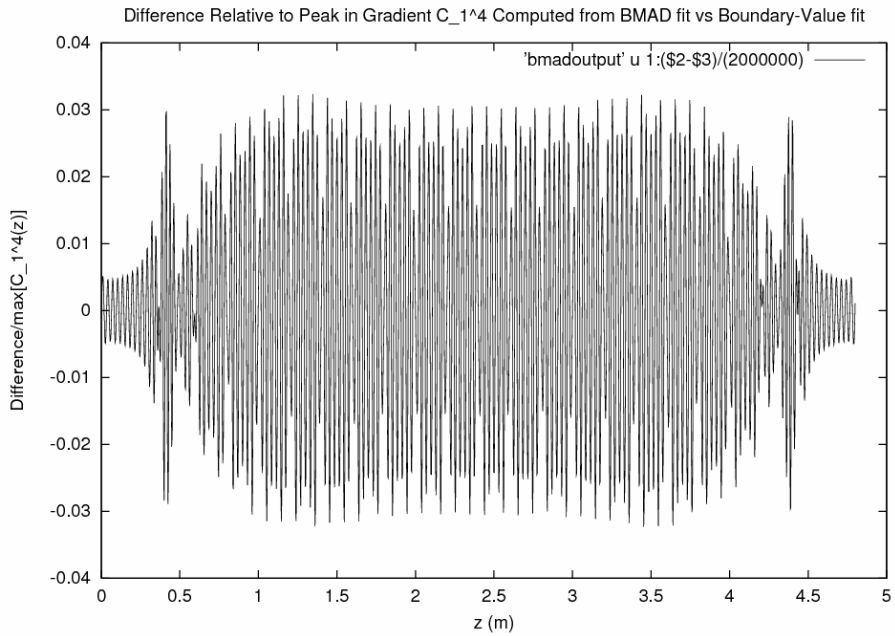
Difference Relative to Peak in Gradient C_1^4 Computed from BMAD fit vs Boundary-Value fit
'bmadoutput' u 1:($2-$3)/(2000000)
Difference/max[C_1^4(z)]
z (m)
0.04
0.03
0.02
0.01
0
-0.01
-0.02
-0.03
-0.04
0
0.5
1
1.5
2
2.5
3
3.5
4
4.5
5

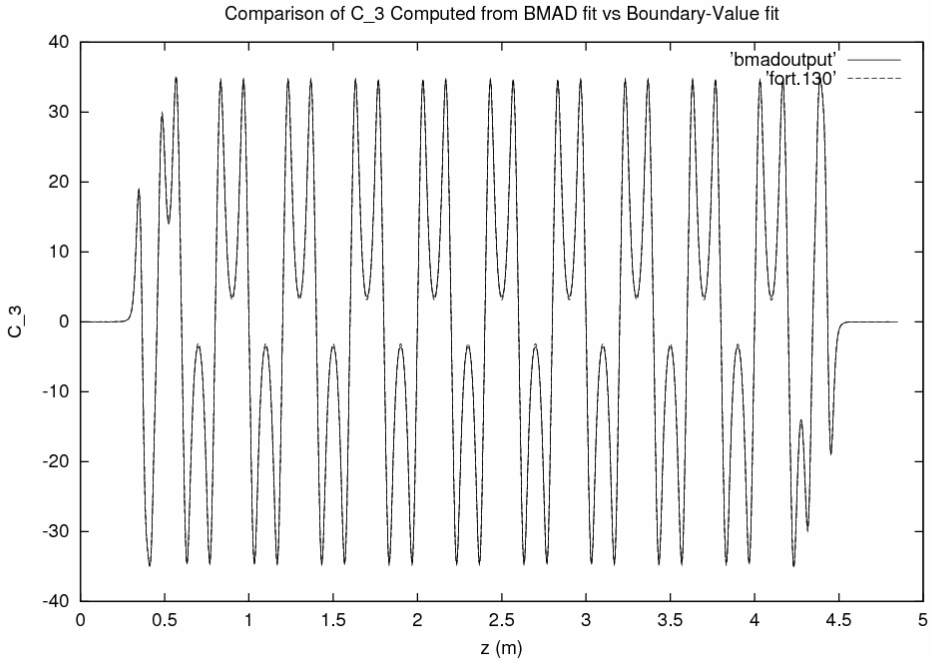
Comparison of C_3 Computed from BMAD fit vs Boundary-Value fit
'bmadoutput'
'fort.130'
C_3
z (m)
40
30
20
10
0
-10
-20
-30
-40
0
0.5
1
1.5
2
2.5
3
3.5
4
4.5
5

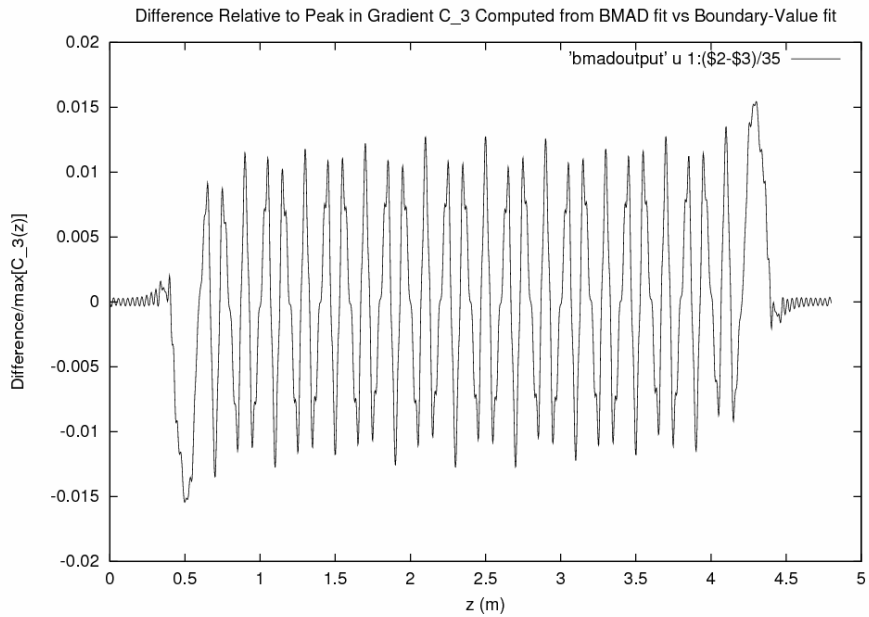
Difference Relative to Peak in Gradient C_3 Computed from BMAD fit vs Boundary-Value fit
'bmadoutput' u 1:($2-$3)/35
Difference/max[C_3(z)]
z (m)
0.02
0.015
0.01
0.005
0
-0.005
-0.01
-0.015
-0.02
0
0.5
1
1.5
2
2.5
3
3.5
4
4.5
5

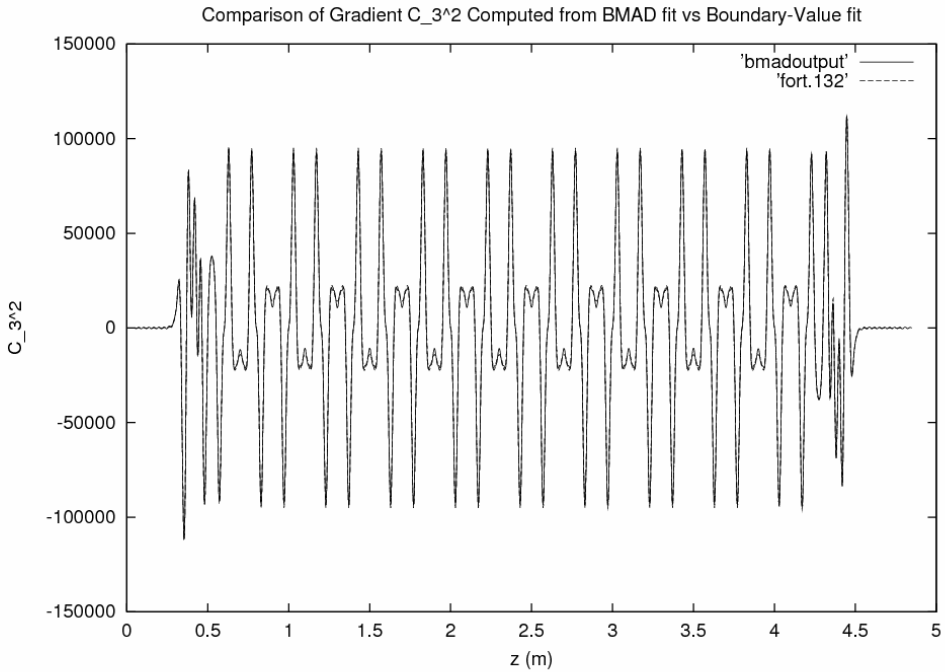
Comparison of Gradient C_3^2 Computed from BMAD fit vs Boundary-Value fit
'bmadoutput'
'fort.132'
C_3^2
z (m)
150000
100000
50000
0
-50000
-100000
-150000
0
0.5
1
1.5
2
2.5
3
3.5
4
4.5
5

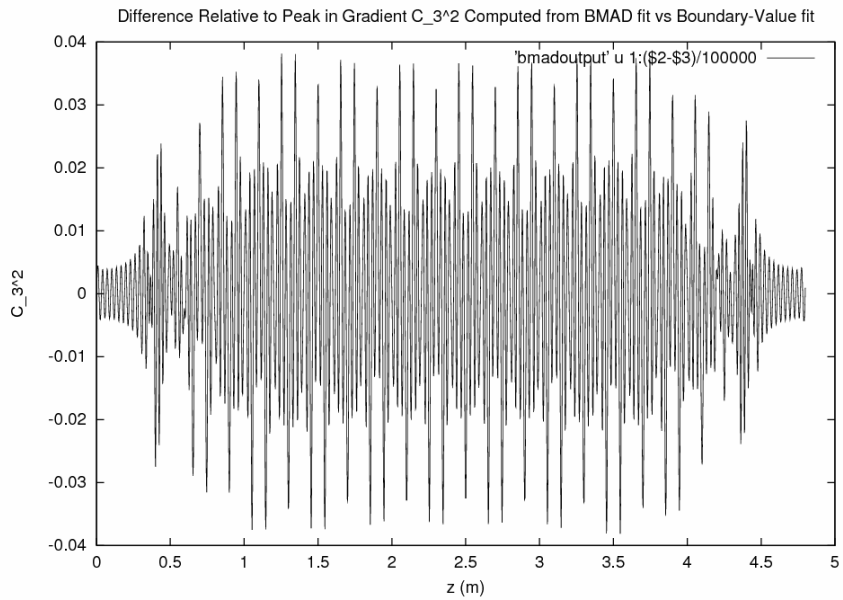
Difference Relative to Peak in Gradient C_3^2 Computed from BMAD fit vs Boundary-Value fit
'bmadoutput' u 1:($2-$3)/100000
C_3^2
z (m)
0.04
0.03
0.02
0.01
0
-0.01
-0.02
-0.03
-0.04
0
0.5
1
1.5
2
2.5
3
3.5
4
4.5
5

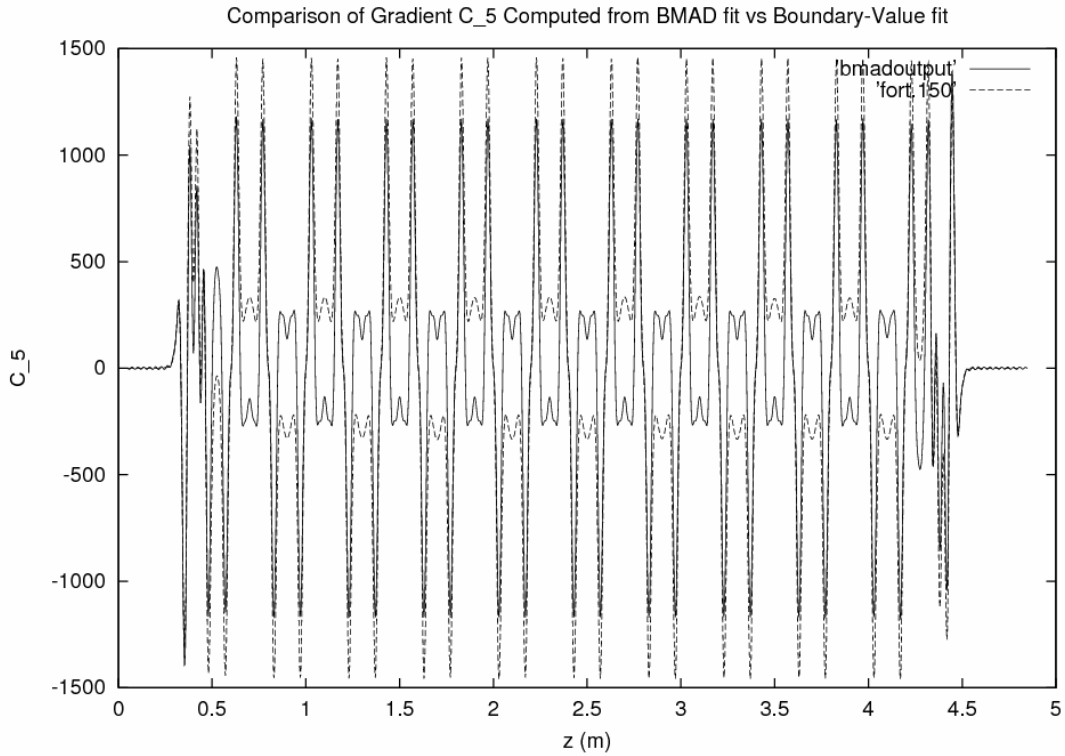

Comparison of on-axis gradient C_5 with the gradient obtained from Cornell's field fit

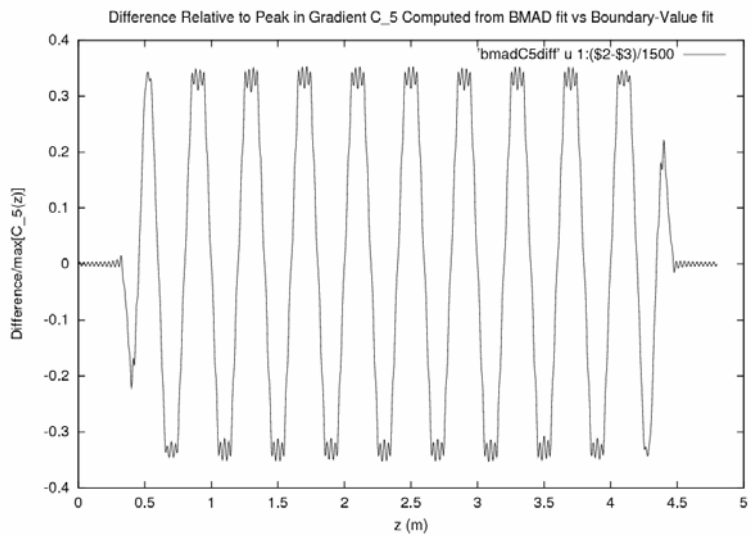

Advantages of Surface Fitting

- Uses functions with known (orthonormal) completeness properties and known (optimal) convergence properties.
- Maxwell equations are exactly satisfied. (Other procedures.)
- Error is globally controlled. The error must take its extrema on the boundary, where we have done a controlled fit.
- Careful benchmarking against analytic results for arrays of magnetic monopoles.
- Insensitivity to errors due to inverse Laplace kernel smoothing. Improves accuracy in higher derivatives. Insensitivity to noise improves with increased distance from the surface: advantage over circular cylinder fitting.

Theory of Smoothing

Note that the gradient = integration of angular Mathieu coefficients against a sequence of weight functions determined by boundary geometry.

$$C_{r,S}^{[m]}(z) = \frac{1}{\sqrt{2\pi}} \frac{i^m}{2^r r!} \int_{-\infty}^{\infty} dk e^{ikz} k^{r+m} \left[\sum_{n=0}^{\infty} \frac{g_s^{2n+1}(k) B_r^{(2n+1)}(k)}{Se'_{2n+1}(u_b, k)} F_{2n+1}(k) \right]$$

$$\propto \int_{-\infty}^{\infty} dk e^{ikz} W_1^{r,m}(k) F_1(k) + \int_{-\infty}^{\infty} dk e^{ikz} W_3^{r,m}(k) F_3(k) + \ldots$$

- Clean angular Mathieu coefficients cut off around k=2/cm. We expect noise to introduce high-frequency contributions to the spectrum of angular Mathieu coefficients $F_m(k)$.
- Kernels (weights) die off quickly for large k, providing an effective cutoff that serves as a low-pass filter to eliminate high-frequency components.
- Insensitivity to noise is improved by choosing geometry such that kernels approach zero quickly.

Wiggler Spectrum

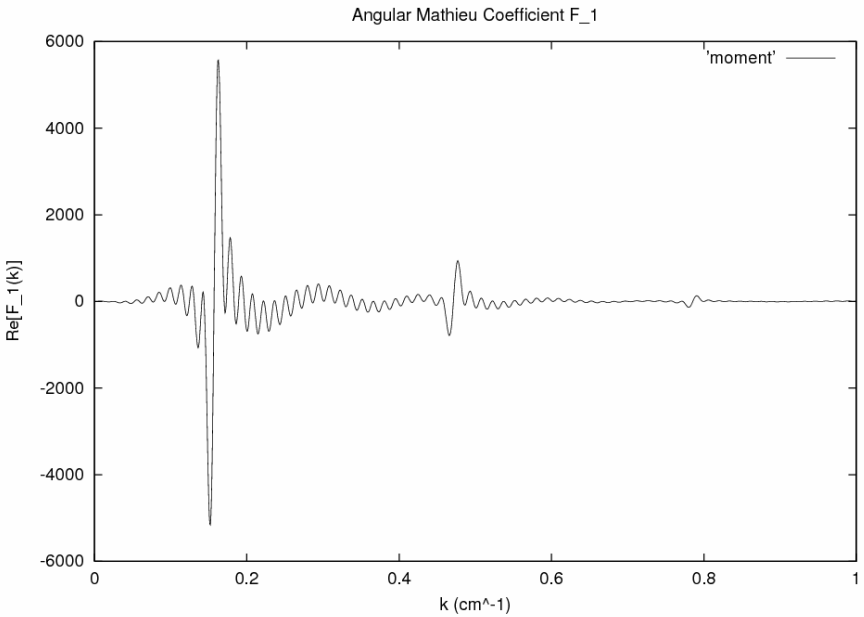

Wiggler period: $L = 40cm$

Peaks occur at frequencies corresponding to odd harmonics $k_n = 2\pi n / L = (0.1571n)cm^{-1}$

Amplitudes fall off by a factor of at least 0.1 for each harmonic; only the harmonics 1,3,5 contribute significantly.

Angular Mathieu coefficient F_1

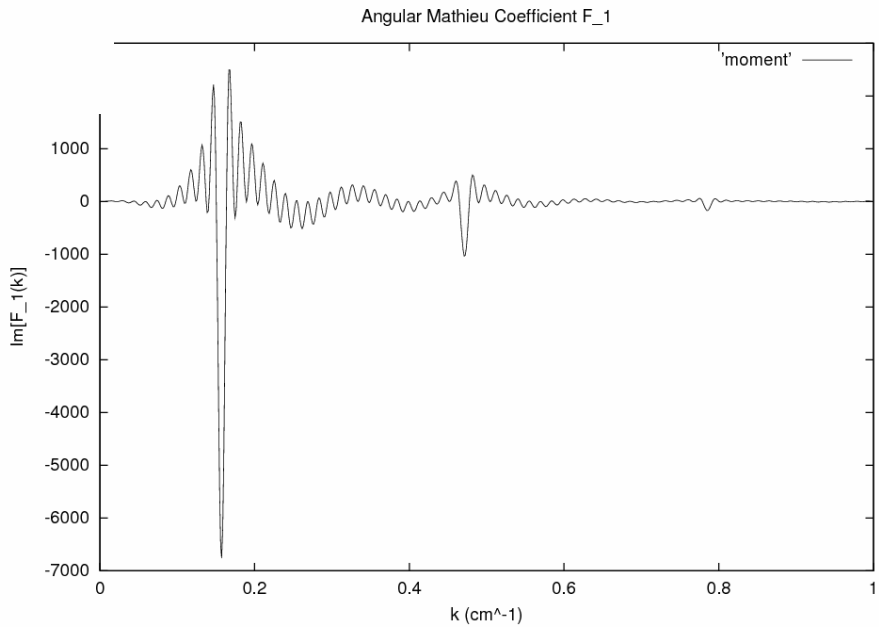

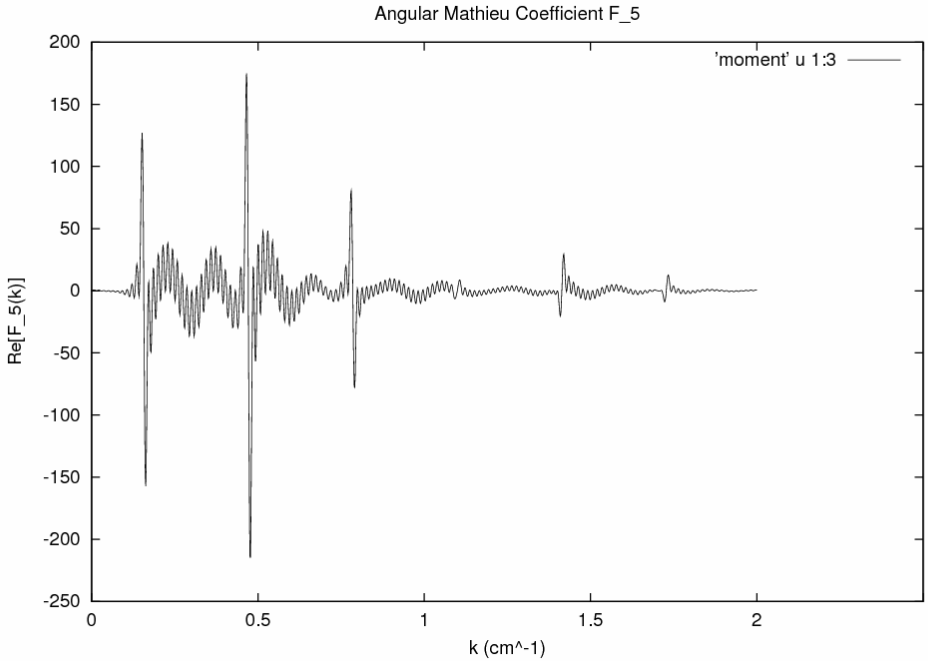

Angular Mathieu coefficient F_5

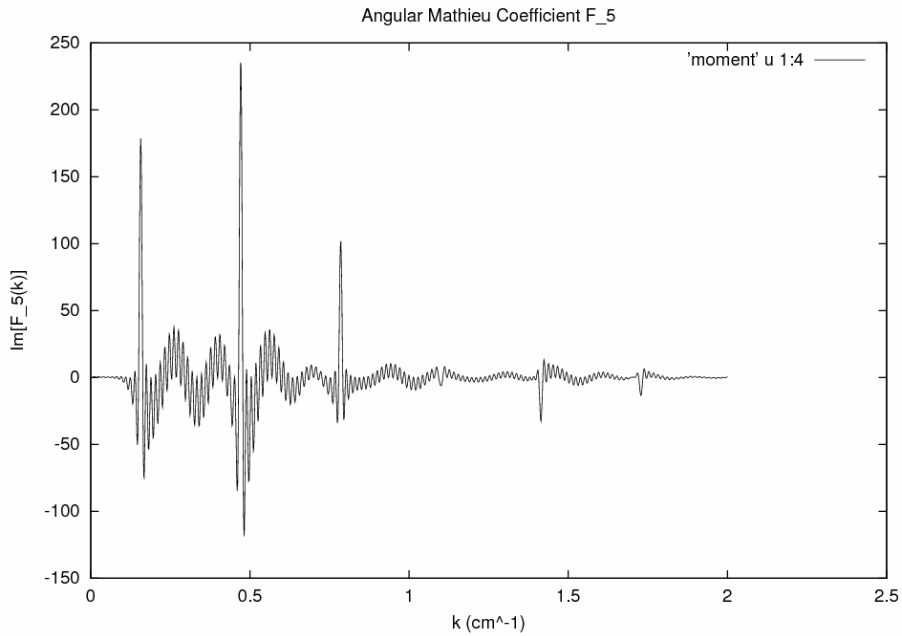

Weight Functions for an Elliptic Cylinder Boundary

- Kernels W corresponding to the lowest 5 moments are plotted.
- Note that these weight functions (kernels) cut off near k=4/cm, with cutoff increasing with order of kernel.
- Nontrivial dependence on k.

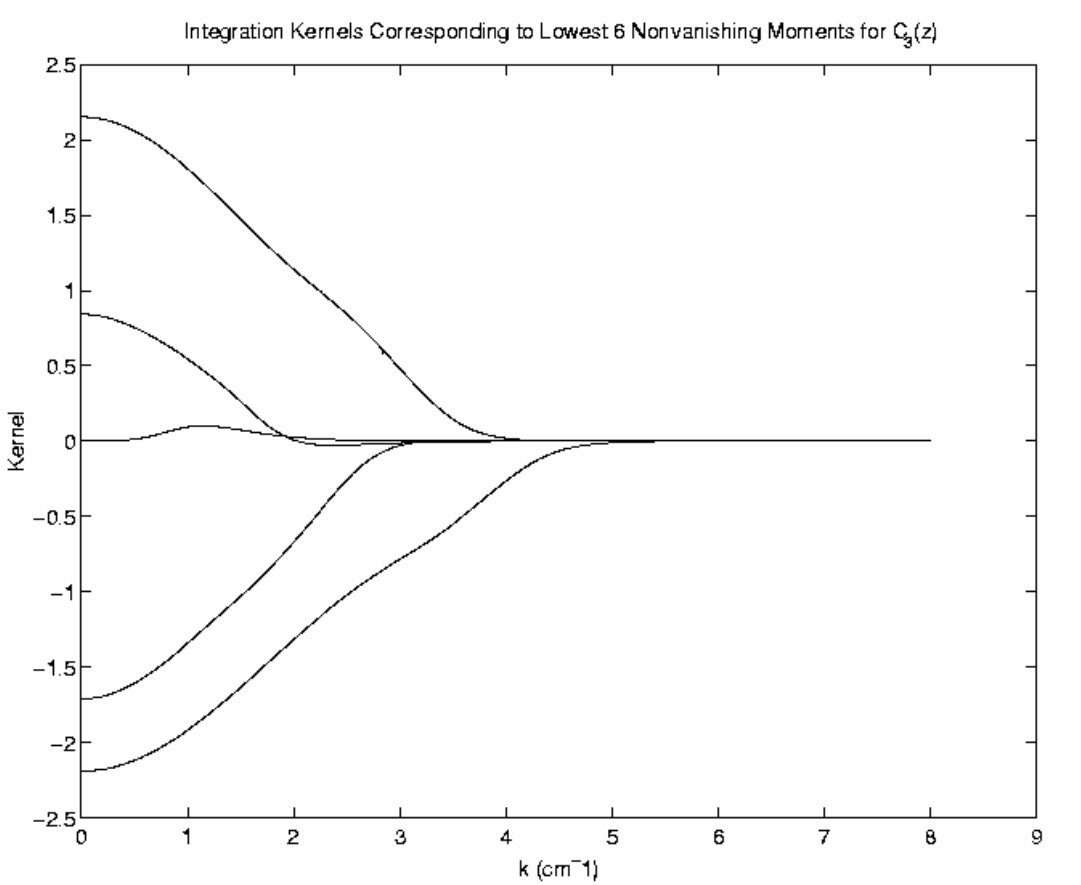

Comparison with Circular Case

There is one kernel for each gradient in the circular case. The kernels for $C_3(z)$ appear below. The circular kernel takes the form $k^2 / I'(kR)$ with R=1.

The first 4 elliptic kernels are shown for the case y_{max}=1, x_{max}=4.

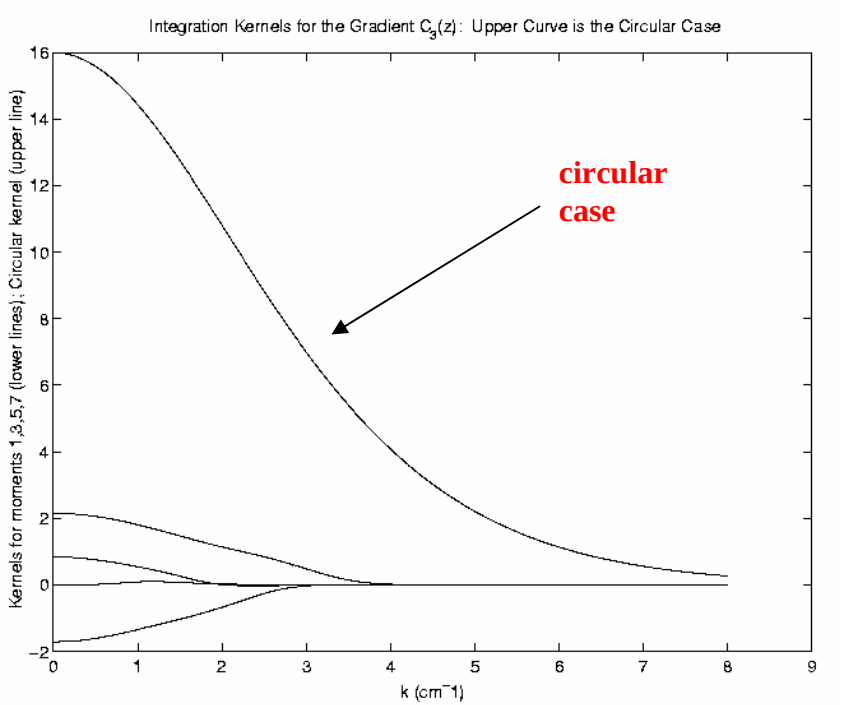

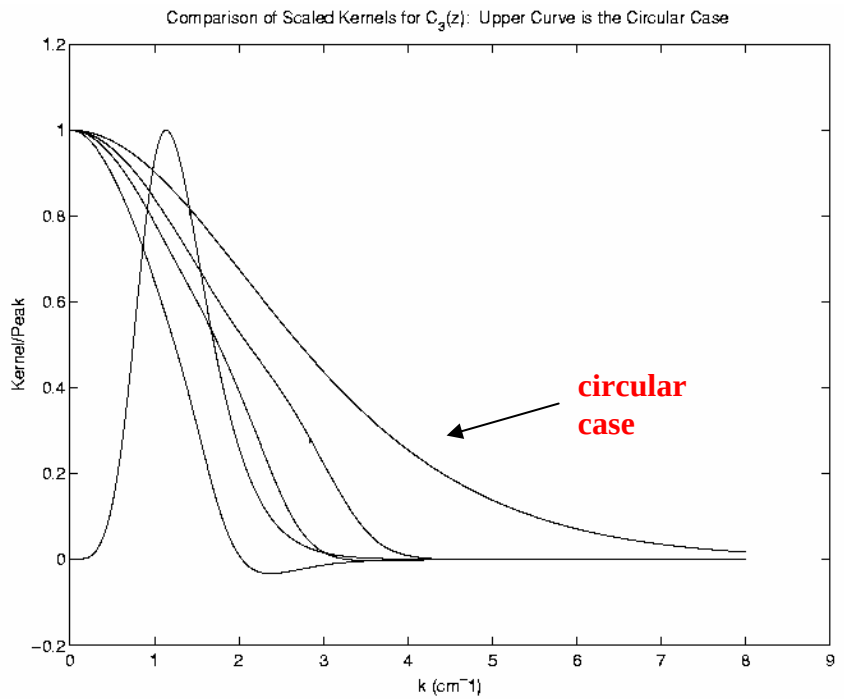

How Does Geometry Affect Smoothing Properties?

We expect accuracy to improve with enclosed cross-sectional area $\propto f^2 \sinh(2u_b)$
Interested in the following limiting behavior.

- Simple Scaling – Fix aspect ratio $y_{\max}/x_{\max} = \tanh(u_b)$ Boundary scales linearly with f.

How do the kernels behave for large focal distance f?

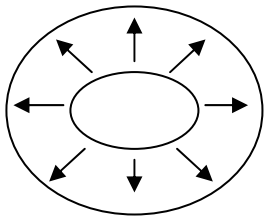

(No clean asymptotic form yet.)

- Elongation – Fix semiminor axis $y_{\max}$ What happens as the semimajor axis grows?

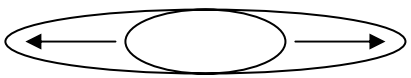

$$\propto k^{2r+2l+1}\sqrt{\pi k}\,B_{2r+1}^{(2n+1)}(k)\sqrt{\frac{y_{\max}}{x_{\max}}}\left(\frac{\sqrt{2}x_{\max}}{y_{\max}}\right)^{4n+4} e^{-kx_{\max}}$$

- Circular – Fix focal length f. As u_b increases, this degenerates to the circular case.

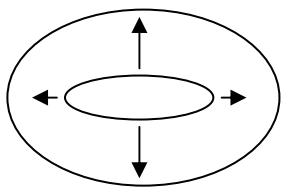

$$k^{2r+2l+1}\sqrt{\frac{2\pi}{kR}}e^{-kR}B_{2r+1}^{(2n+1)}(k)$$

Gradient C_5(z) Computed Using 5/3 Aspect Ratio Domain

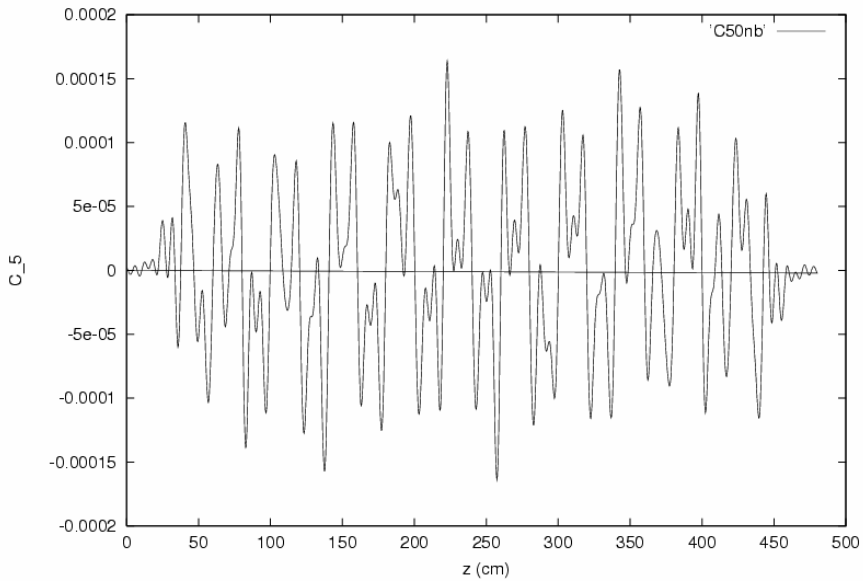

Effect of domain size on smoothing

(xmax,ymax)=(1,0.6)cm a.r.=5/3

(xmax,ymax)=(4.4,0.6)cm a.r.=22/3

(xmax,ymax)=(4.4,2.4)cm a.r.=11/6

Gradient C_5(z) Computed Using 22/3 Aspect Ratio Domain

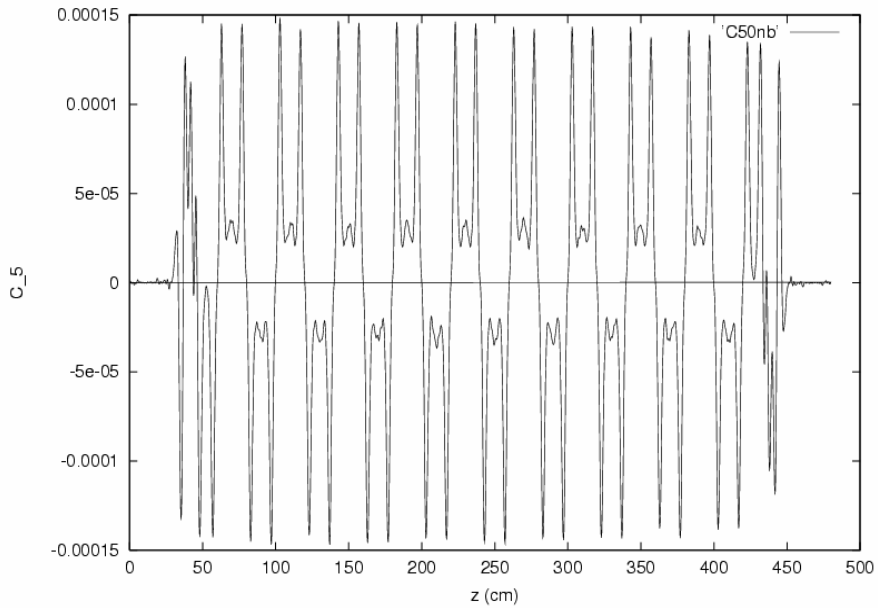

Gradient C_5(z) Computed Using 11/6 Aspect Ratio Domain